Do Magnetite Layers In Algoma-Type Banded Iron Formations (BIF) Preserve Their Primary Geochemical Signature? A Case Study of Samples From Three Archean BIF-Hosted Gold Deposits

Blandine Gourcerol, Daniel Kontak, Phillips Thurston, Quentin Duparc

HAL Id: hal-02267547
https://hal.archives-ouvertes.fr/hal-02267547

Submitted on 11 Sep 2019

DO MAGNETITE LAYERS IN ALGOMA-TYPE BANDED IRON FORMATIONS (BIF) PRESERVE THEIR PRIMARY GEOCHEMICAL SIGNATURE? A CASE STUDY OF SAMPLES FROM THREE ARCHEAN BIF-HOSTED GOLD DEPOSITS

Blandine GOURCEROL[§], Daniel J. KONTAK, and Phillips C. THURSTON

Mineral Exploration Research Centre, Laurentian University, Sudbury, Ontario, Canada P3E 2C6

Quentin DUPARC

Université du Québec à Chicoutimi, Chicoutimi G7H 2B1, Québec, Canada

Abstract

The geochemistry of chert layers in Algoma-type banded iron formations (BIF) has been used to constrain the depositional setting of the BIFs, as rare earth element (REE) and yttrium (Y) systematics are a function of their chemical environment of formation. In contrast, the chemistry of the interbedded oxide-rich layers (*i.e.*, magnetite) has not been analyzed for this purpose because of the presumed potential effects related to diagenetic changes during conversion from primary iron-bearing mineralogy to magnetite. Here, we explore the validity of this latter hypothesis by examining the results of LA-ICP-MS analysis of iron-oxide layers at three Canadian BIF-hosted gold deposits (*i.e.*, Meadowbank, Meliadine, Musselwhite) to assess whether the primary REE+Y systematics of the oxide layers are preserved and, if so, what are the implications. The results indicate that, regardless of their diagenetic, later metamorphic, and hydrothermal histories, the chemistry of the iron oxides retains a primary signal in all cases with the following indicated: (1) interaction of the primary Fe-oxyhydroxide phases with seawater, as reflected by heavy REE enrichment relative to light REE depletion that is coupled with variable La and Y enrichment; and (2) some input of moderate-temperature (>250 °C) hydrothermal vent fluids, as suggested by positive Eu anomalies. The chemical data are also used to evaluate currently used classification diagrams for ore deposits based on magnetite chemistry. Our new data indicate that the fields for magnetite geochemistry in BIF are too restricted or lead to misclassification of samples. In the case of the latter, it may be that interaction of fluids with the immediate substrate influences the chemical signature of samples. Therefore, caution is suggested in using these diagrams where hydrothermal fluids are involved in magnetite formation.

Keywords: magnetite, banded iron formation, geochemistry, hydrothermal, seawater.

Introduction

Algoma-type banded iron formations (BIFs) are thinly bedded, chemical sedimentary rocks comprised of alternating layers of iron-bearing minerals and chert. The iron-bearing minerals are considered to have originally precipitated as iron oxyhydroxides due to mixing of acidic to neutral, iron-rich Archean seawater and alkaline moderate-temperature hydrothermal fluids (Shibuya *et al.* 2010, Gourcerol *et al.* 2015b) combined with possible photoautotrophic bacterial activity (*i.e.*, Kappler *et al.* 2005, Konhauser *et al.* 2005, Gourcerol *et al.* 2015b). These primary iron-bearing minerals are transformed during diagenesis or by later metamorphic recrystallization to hematite, magnetite, various iron-silicates and carbonates, and pyrite (*e.g.*, Posth *et al.* 2013). The interbedded chert layers have been shown to reflect a primary geochemical signature that suggests precipitation upon interaction of seawater and moderate-temperature hydrothermal fluids with variable amounts of detrital contamination (*e.g.*, Gourcerol *et al.* 2015a, b, c). An essential question in this regard, therefore, is whether the iron-bearing minerals, despite having experienced multiple recrystallization events (*e.g.*, Pickard *et al.* 2003), retain a geochemical signature indicative of their primary environment, this being a

---

[§] *Corresponding author e-mail address*: gourcerol.blandine@gmail.com

//titan/production/c/cami/live_jobs/cami-54/cami-54-03/cami-54-03-11/layouts/cami-54-03-11.3d
■ 4 January 2017 ■ 10:28 am ■ Allen Press, Inc.

Page 1

combination of marine seawater and hydrothermal vent fluids.

The compositional variability of oxide minerals (*e.g.*, magnetite, hematite), which collectively form in a wide variety of ore-forming environments (*e.g.*, hydrothermal *versus* magmatic), has been the focus of many studies in recent years, in part due to advances in analytical instrumentation such as the laser ablation-inductively coupled plasma-mass spectrometer (LA-ICP-MS) (*e.g.*, Grigsby 1990, Dare *et al.* 2012, 2014, Nadoll *et al.* 2014). Of particular significance is that several studies have demonstrated that the geochemical signature of the oxide minerals, in particular magnetite, can be a genetic indicator of ore deposit environments, in part due to the ability of the analytical method to provide the resolution necessary to distinguish various geochemical types (Dupuis & Beaudoin 2011, Dare *et al.* 2014). As a result of these recent advances, it is now possible to distinguish geochemically between hydrothermal and magmatic magnetite. For example, whereas hydrothermal magnetite compositions may vary depending on various factors such as fluid composition, host rock buffering, and re-equilibration processes (Nadoll *et al.* 2014), they are generally characterized by depletion in Ti and an elevated Ni/Cr ratio compared to their magmatic equivalent and are enriched in elements which do not nominally enter the lattice of magmatic magnetite (*e.g.*, Si and Ca). Magmatic magnetite is enriched in Ti with a lower Ni/Cr ratio (Dare *et al.* 2014). However, despite geochemical characteristics which have not been well documented, magnetite may also be precipitated by hydrogeneous processes during formation of BIF, as discussed above (*e.g.*, Kappler *et al.* 2005, Konhauser *et al.* 2005, Shibuya *et al.* 2010, Gourcerol *et al.* 2015b) and may show depletion in compatible elements (Cr, Ni, V, Co, Zn, Ti) that are characteristic of magnetite formed from low-temperature environments (Dare *et al.* 2014).

Only a few studies have explored the REE geochemistry of iron oxides in Algoma-type BIF (*e.g.*, Pecoits *et al.* 2009, Angerer *et al.* 2012, Li *et al.* 2014), but in such cases, analyses of the accompanying chert bands are lacking. These analyses would provide an internal check on geochemical concordance, that is, each providing the same chemical signature of their environment of formation. Thus, the occurrence of geochemical parallelism and hence genetic processes between the chemistry of magnetite and chert (*i.e.*, LREE depletion relative to HREE, variable positive La/La* and Y/Y* anomalies, positive Eu/Eu* anomalies) has yet to be documented. The purpose of this paper is to present the first such data and validate this hypothesis.

In this contribution, we explore the geochemistry of iron-oxide layers at three Archean BIF-hosted gold deposits located in Canada: the ∼4 Moz Au Meadowbank deposit, hosted by the 2.71 Ga Woodburn Lake greenstone belt; the ≥2.8 Moz Au Meliadine gold district, hosted by the 2.6 Ga Rankin Inlet greenstone belt; and the ∼6 Moz Au Musselwhite deposit, hosted by the 2.9–3 Ga North Caribou greenstone belt. Importantly, in each of these studied areas we have previously characterized the chemistry of the inter-bedded chert (Fig. 1; Gourcerol *et al.* 2015a, b, c). Also relevant is that the BIFs at each of these deposits are either intercalated with mafic to ultramafic volcanic rocks or associated interflow sedimentary rocks, which may represent different potential sources for the iron-rich minerals composing the Fe-oxide layers.

The main objective of this study is, therefore, to assess the potential of using the REE + Y systematics of magnetite bands to identify their primary geochemical signature, as we have done for the associated cherts (Gourcerol *et al.* 2015b). If this study is successful, it will provide the possibility of using the geochemistry of magnetite from magnetite-rich bands to constrain the genesis of BIF units. In addition, we also use these data to assess the validity of the currently defined field for magnetite from BIF settings in chemical classification diagrams.

GEOLOGICAL SETTING OF THE SELECTED BIFS

The Meadowbank gold deposit

The Meadowbank deposit, which has been mined since 2010, contains a total of about 4 Moz of gold including 1.3 Moz produced from 2010 to 2013 (Janvier *et al.* 2015). Located in the Rae Domain of the Churchill Province, the deposit is hosted by the Woodburn Lake greenstone belt (*ca.* 2.71 Ga) which consists of tholeiitic and komatiitic metavolcanic rocks with minor calc-alkaline felsic tuffs and flows with intercalated BIF and clastic metasedimentary rocks (Armitage *et al.* 1996, Sherlock *et al.* 2001a, b, 2004, Hrabi *et al.* 2003, Pehrsson *et al.* 2004). The regional metamorphic grade ranges from middle greenschist to amphibolite facies (Pehrsson *et al.* 2004) and the sequence was deformed by at least six regional-scale Archean and Paleoproterozoic deformation events (*e.g.*, Pehrsson *et al.* 2013).

Numerous units of oxide-, silicate-, and locally sulfide-facies Algoma-type BIF have been identified which include the West IF, Central BIF, and East BIF; all of the BIFs are generally interlayered with the volcanic rocks and locally with a quartzite unit (Gourcerol *et al.* 2015c, Sherlock *et al.* 2001a, b, 2004).
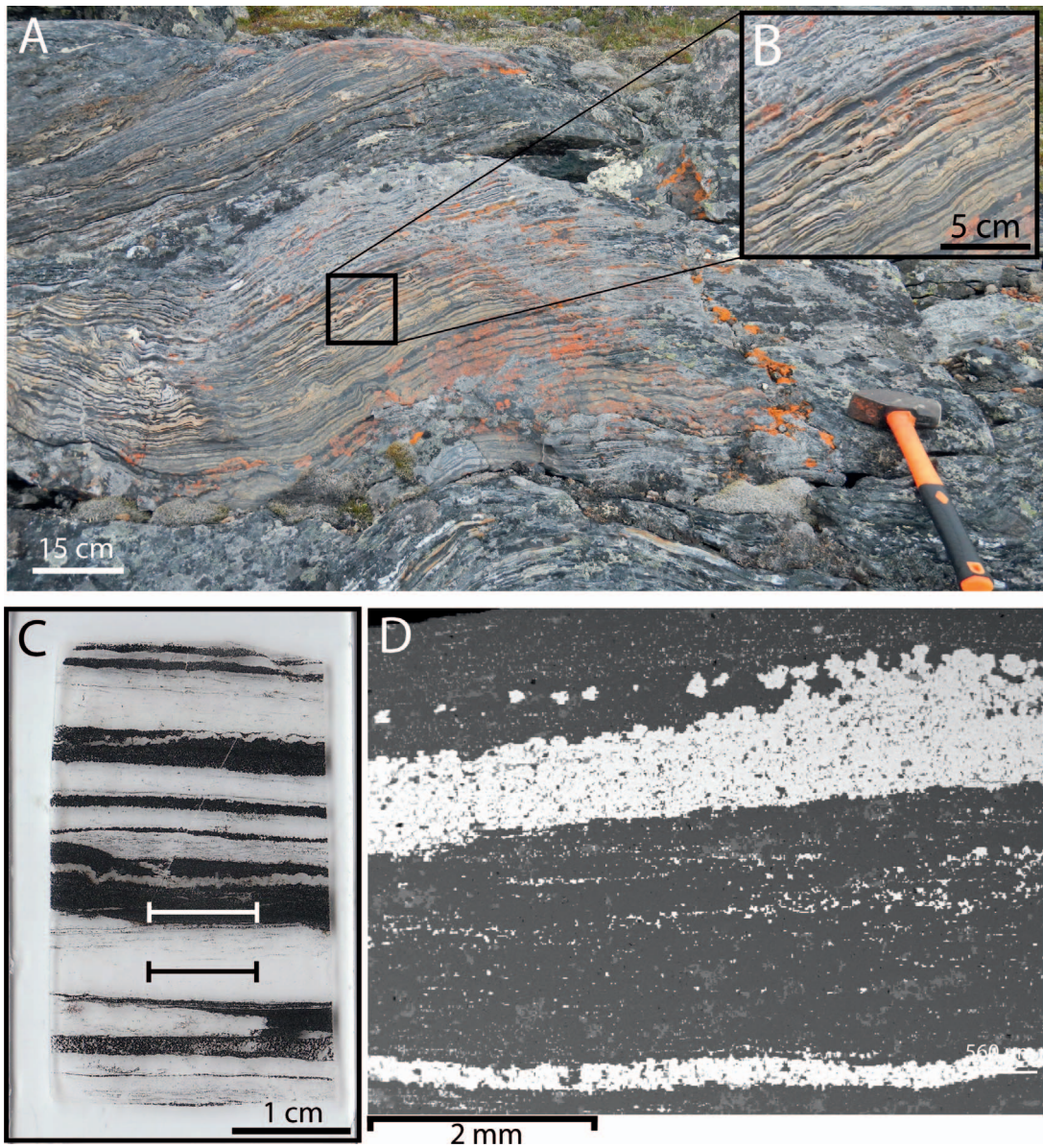
FIG. 1. Photographs at different scales that illustrate the nature of the BIFs in the field, their microscopic features and traces of the laser ablation traverses. (A) Outcrop photograph of BIF at the Meadowbank gold deposit area showing the characteristic layers of chert and iron-rich layers, in this case magnetite. (B) Close up of the outcrop showing alternating layers of chert and magnetite. (C) Scanned thin section of BIF from outcrop in image which shows the chert and magnetite layers. The black solid line represents the laser ablation traverse done on the chert as part of our previous LA ICP-MS study (Gourcerol *et al*. 2015a, b, c), whereas the white solid line represents the line traverse done on the magnetite rich layer in this study. (D) SEM back-scattered electron image of the BIF layering showing alternating layers of chert and magnetite.

The Meliadine gold district

The Meliadine gold district, which is one of the Canada's largest BIF-hosted gold districts, contains 2.8 Moz Au in reserves as well as an indicated and inferred resource of 5.8 Moz Au (Lawley *et al*. 2015). The gold district is hosted by the 2.6 to 2.7 Ga Rankin Inlet greenstone belt (Wright 1967, Aspler & Chiarenzelli 1996a) which lies along the boundary between the Central and the North Western Hearne domains of the Churchill Province (Tella *et al*. 2007, Davis *et al*. 2008). The Rankin Inlet greenstone belt consists of poly-deformed massive and pillowed mafic volcanic rocks, felsic pyroclastic rocks and associated interflow sedimentary units, gabbro sills, and oxide-facies BIFs; all of these units are intruded by minor granite and undeformed biotite lamprophyre, as well as late gabbro and diabase dikes of Archean and Proterozoic age. These rocks have been metamorphosed from lower greenschist to lower-middle amphibolite facies (Carpenter 2004, Carpenter, *et al*. 2005).

The Musselwhite gold deposit

The Musselwhite deposit, which has been mined since 1997, contains a total of about 6 Moz of gold, including 4 Moz produced and 1.85 Au reserves (Oswald *et al*. 2015). Located in the North Caribou terrane of the Superior Province, the deposit is hosted by the North Caribou greenstone belt which is dominated by mafic to ultramafic metavolcanic rocks of the 2973 to <2967 Ma Opapimiskan-Markop metavolcanic assemblage, and tholeiitic basalts and minor felsic volcanics of the 2980 to 2982 Ma South Rim metavolcanic assemblage (Biczok *et al*. 2012, McNicoll *et al*. 2013). These rocks have been metamorphosed from lower greenschist to lower-mid amphibolite facies (Breaks *et al*. 2001) and deformed by three deformation events (Hall a& Rigg 1986, Breaks *et al*. 2001). The Opapimiskan-Markop metavolcanic assemblage consists, from the structural base to the top, of the "Lower Basalt" unit, the Southern Iron Formation, "Basement Basalt" unit, and the Northern Iron Formation (*e.g*., Moran 2008, Biczok *et al*. 2012). The nature of the BIFs is described in more detail in Gourcerol *et al*. (2015a).

Sample Description, Analytical Methods, and Data Treatment

The samples collected for the study include: (1) seven samples from the Meadowbank deposit (Fig. 1A, B); (2) eight samples from the Meliadine gold district; and (3) three samples from the Musselwhite deposit. These samples represent bands of Fe-oxides (Fig. 2A, B, C, D) that are mainly composed of anhedral and amalgamated (*i.e*., polycrystalline texture of anhedral and annealed crystals) magnetite with rare cryptocrystalline hematite that is locally overprinted by late euhedral magnetite grains. The iron-rich bands form millimetric to centimetric layers that are interbedded with chert layers. The Fe-oxide layers are dominated by magnetite, but they may also contain variable proportions of mineral inclusions such as quartz, hematite, pyrite, pyrrhotite, apatite $\pm$ chlorite, and variable silicates (Fig. 2A, B, C, D). No specific attention was paid to recognition of and deciphering the different events responsible for the formation of the Fe-oxide layers, that is, primary *versus* later recrystallization stages, as only the continuous Fe-oxides layers (*i.e*., anhedral and amalgamated magnetite phase) were selected for analysis.

Each of the Fe-oxide layers analyzed in this study is located immediately adjacent to the chert layers analyzed in our earlier study (Gourcerol *et al*. 2015b; Fig. 1C, D). Polished thin sections (100 μm thick) were examined, using both transmitted and reflected light microscopy, and selected material was studied in more detail using a JEOL JSM-6400 scanning electron microscope coupled to an energy dispersive spectrometer (EDS). Based on previous petrographic work, areas for analysis were selected to minimize the presence of phases other than magnetite, including alteration, and mineral inclusions. Operating conditions were an accelerating voltage of 20 keV, 1.005 nA beam current, acquisition count times of 10 s, and a working distance of 15 mm. The SEM-EDS was used to select the most suitable magnetite layers having minimal amounts of paragenetically later-stage minerals related to metamorphic, hydrothermal, or ore-forming processes, such as garnets, variable amphiboles, and sulfides.

Using the same protocol applied to the chert layers analyzed in Gourcerol *et al*. (2015a, b, c), the magnetite layers were analyzed with line traverses rather than spots (Fig. 2E, F) using a Resonetics RESOlution M-50 193 nm ArF excimer laser-ablation system coupled to a Thermo X Series II quadrupole ICP-MS in a two-volume Laurin Technic sample cell. The instrument operated with a forward power of 1450 W. Gas flows were 800 ml/min for Ar, 650 ml/min for He, and 6 ml/min for N. Dwell times for elements analyzed were 10 ms. These conditions should minimize interferences such as ^{69}Ga with ^{29}Si^{40}Ar. Stage movement speed was 20 μm/s. As chert and magnetite layers show very low concentrations of REE, spot analyses may yield data below the detection limit for many elements, therefore, line traverses of polycrystalline aggregates were made using both 140 and 190 μm beam diameters with a repetition rate of

10 Hz and an energy density of 7 J/cm^2 to optimize the time-signal acquisition, representing therefore an average for each element along the analyzed traverse. However, since the line traverse method increases the possibility of detrital contaminants, present as inclusions or minerals disseminated along the traverse line, the Queensland alluvial shale composite (MUQ) was used to normalize the REE + Y values to minimize the influence of any potential terrigenous input, whereas trace elements were normalized to bulk continental crust (values from Rudnick & Gao 2003). The MUQ composition represents a mixed bimodal felsic and mafic volcanic provenance (Kamber *et al.* 2005), which acts as a proxy for the expected average terrigenous input from a typical bimodal greenstone belt into the Archean ocean (*e.g.*, Bolhar *et al.* 2005, Thurston *et al.* 2012).

The final concentrations of elements were determined using off-line calculations following the protocol of Longerich *et al.* (1996). Data were processed with Iolite (Paton *et al.* 2011) and the NIST 612 glass standard was used as a primary external reference material (*e.g.*, Nadoll *et al.* 2014); iron concentrations were used as an internal standard for calibration of the LA-ICP-MS data.

The elemental concentrations reported in this study represent the integrated signal over the length of the traverse. The element list used for each analysis included the 14 REEs in addition to [7]Li, [9]Be, [29]Si, [45]Sc, [47]Ti, [51]V, [52]Cr, [55]Mn, [57]Fe, [59]Co, [60]Ni, [65]Cu, [66]Zn, [69]Ga, [75]As, [85]Rb, [88]Sr, [90]Zr, [93]Nb, [95]Mo, [107]Ag, [111]Cd, [115]In, [118]Sn, [121]Sb, [133]Cs, [137]Ba, [178]Hf, [181]Ta, [182]W, [197]Au, [205]Tl, [208]Pb, [232]Th, and [238]U. In this study, the detection limits achieved were significantly lower than the concentration of REEs in magnetite samples (Tables 1, 2, 3). The La, Ce, Eu, and Y anomalies were calculated [Equations (1) to (4)] following the procedure of Lawrence & Kamber (2006):

$$(La/La)^*_{MUQ} = La_{MUQ}/\left[Pr_{MUQ}*(Pr_{MUQ}/Nd_{MUQ})^2 \right] \tag{1}$$

$$(Ce/Ce)^*_{MUQ} = Ce_{MUQ}/\left[Pr_{MUQ}*(Pr_{MUQ}/Nd_{MUQ}) \right] \tag{2}$$

$$(Eu/Eu)^*_{MUQ} = Eu_{MUQ}/(Sm^2_{MUQ}*Tb_{MUQ})^{1/3} \tag{3}$$

$$(Y/Y)^*_{MUQ} = Y_{MUQ}/(0.5Er_{MUQ}*0.5Ho_{MUQ}) \tag{4}$$

The Gd values in Archean iron formation are considered to reflect a combination of a small positive Gd anomaly associated with seawater (Bau & Dulski

1996) and a slightly negative Gd anomaly associated with hydrothermal vent fluid (*e.g.*, Allwood *et al.* 2010). Thus, as Archean seawater was influenced by hydrothermal vent fluids, the Gd anomalies are variable in magnitude and sign (+ *versus* −), suggesting precipitation under influence of seawater and hydrothermal input. We note that the Gd anomalies reported and discussed in previous papers on REE + Y systematics from BIF precipitated in Archean seawater (*e.g.*, Bolhar *et al.* 2005, Thurston *et al.* 2012) were small to nonexistent, thus Gd anomalies are not discussed here.

REE + Y Systematics

Despite some minor exceptions, the REE + Y normalized data presented in the tables (Tables 1, 2, 3) and diagrams (Fig. 3) show relatively uniform REE + Y patterns for the magnetite layers sampled from the three different gold deposits (*i.e.*, Meadowbank, Meliadine, and Musselwhite) and these data are discussed separately below. Comparisons to other studies of magnetite geochemistry are discussed in subsequent sections.

In the Meadowbank area (Fig. 3A), the magnetite bands show depletion in light REE (LREE) relative to middle and heavy REE (HREE) with Nd/Yb$_{MUQ}$ = 0.1–0.4 associated with slight to moderate positive La, Y, and Eu anomalies (La/La*$_{MUQ}$ = 1.4–2.7, Y/Y*$_{MUQ}$ = 1.01–1.6, Eu/Eu*$_{MUQ}$ = 1.7–3.7) and super-chondritic Y/Ho values (Y/Ho = 30.9–43.9). In addition, slight positive Ce anomalies are notable (Ce/Ce*$_{MUQ}$ = 1.09–1.38).

In the Meliadine gold district (Fig. 3B), most of the magnetite layers also show depletion in the LREE relative to middle and HREE (Nd/Yb$_{MUQ}$= 0.08– 0.6) with associated slight to moderate positive La, Y, and Eu anomalies (La/La*$_{MUQ}$ = 0.7–1.8, Y/Y*$_{MUQ}$ = 0.9– 1.3, Eu/Eu*$_{MUQ}$ = 0.9–1.9) and super-chondritic to chondritic Y/Ho values (Y/Ho = 24.7–34.9). In detail, samples MEL-032 and MEL-033 yield slightly anomalous HREE-depleted concentrations (Nd/Yb$_{MUQ}$= 1.4–1.9) which are also associated with moderate positive La, Y, and Eu anomalies. Minor to moderate positive Ce anomalies are also recognized in these samples (Ce/Ce*$_{MUQ}$ = 0.9–1.2).

In the Musselwhite area (Fig. 3C), magnetite layers show depletion in LREE relative to middle and HREE (Nd/Yb$_{MUQ}$= 0.3–0.5) with associated slight to moderate positive La, Y, and Eu anomalies (La/La*$_{MUQ}$ = 1.14–2.45, Y/Y*$_{MUQ}$ = 1.2–1.6, Eu/Eu*$_{MUQ}$ = 2.1–2.8), super-chondritic Y/Ho values (Y/Ho = 35.8–41.3), and slightly to moderately positive Ce anomalies (Ce/Ce*$_{MUQ}$ = 1.1–1.3).
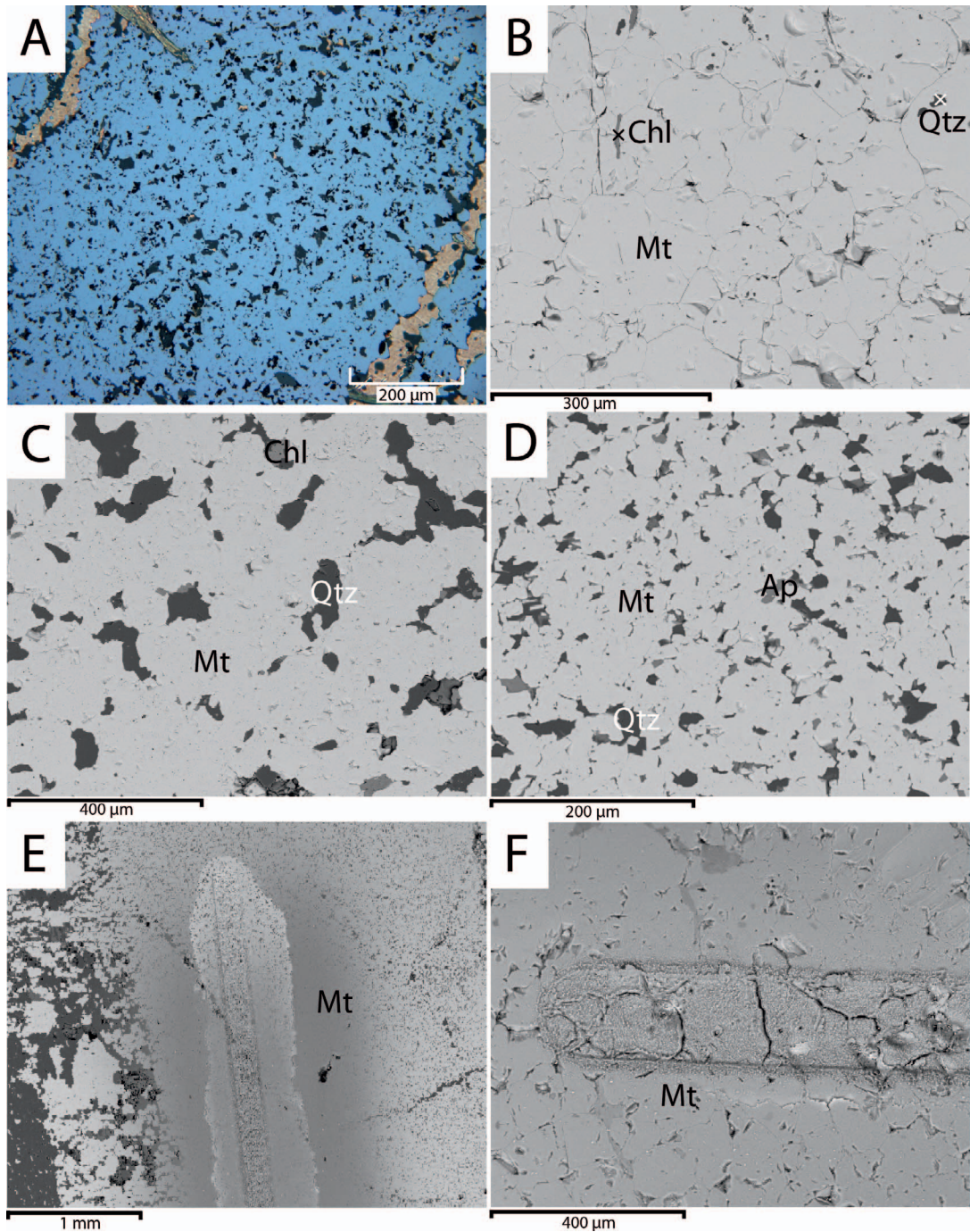
Fɪɢ. 2. Images showing typical Fe-oxide layers sampled for this study: (A) Reflected light image of a polished thin section of sample AMB-126225 showing its groundmass which consists of magnetite with minor quartz (yellowish color) and minor recrystallized magnetite ±hematite (darker grey) inclusions. (B) Back-scattered electron (BSE) image from the SEM of sample MEL-025 which illustrates a magnetite band with inclusions of minor chlorite and quartz. (C) BSE image from the SEM of sample MEL-028 which illustrates magnetite layers associated with minor inclusions of quartz and chlorite. (D)

//titan/production/c/cami/live_jobs/cami-54/cami-54-03/cami-54-03-11/layouts/cami-54-03-11.3d
■ 4 January 2017 ■ 10:28 am ■ Allen Press, Inc.

Page 6

Additional Major and Trace Element Data

Magnetite layer samples from the three deposits show relatively similar abundances of major and trace elements, as indicated in Figure 4, which attests to their similar overall geochemistry. As expected, high concentrations of Fe, Ti, V, Cr, Mn, Ni, and Zn occur in the magnetite, whereas the relatively high Si concentrations, as noted in the three deposits, are attributed to the presence of quartz and other silicate grains present along the line traverses. The moderate concentrations of Ba and Sr detected may reflect the presence of feldspar, likely of metamorphic origin.

In previous geochemical studies of magnetite, data were normalized to bulk continental crust (values from Rudnick & Gao 2003) in order to emphasize the partitioning behavior of the trace elements between the magnetite, magma, hydrothermal fluid, and co-crystallizing phases (Dare et al. 2014). Therefore, in order to assess and compare the trace element data from this study to that of other magnetite studies, the data for our samples have also been normalized to bulk continental crust in multi-element variation diagrams in which elements are plotted in order of increasing compatibility with respect to magnetite (Dare et al. 2014). Most of the major and trace elements show consistent patterns (Fig. 5A, B, C) with concentrations less than one times bulk continental crust. In detail, however, the magnetite samples from the Meadowbank, Meliadine, and Musselwhite deposits show slight to moderate relative depletions in Ti, Co, V, Ni, and Cr compared to magnetite of high-temperature origin (Dare et al. 2014). This latter feature is in general similar to the data for both whole-rock (Pecoits et al. 2009, Angerer et al. 2012) and in situ (Dare et al. 2014, ~~Dupuis et al. 2014,~~ Nadoll et al. 2014) analyses of magnetites from BIFs in the literature (Fig. 5A, B, C). It must be noted that the composition of iron formations associated with gold mineralization do not differ substantially from non-mineralized iron formations (e.g., Gourcerol et al. 2015c, Thurston et al. 2012). Compared to the relatively high-temperature (i.e., >500 °C) hydrothermal magnetite samples of Dare et al. (2014), the magnetites in this study formed in part from lower-temperature fluids, including a component of hydrothermal vent fluids (<250 °C). Thus, based on the latter, it is not surprising that the

BIF magnetites are notably depleted in these compatible elements (Fig. 5), which is probably a reflection of their lower solubility in these fluids (e.g., Ray & Webster 2007, Nadoll et al. 2012, 2014, Dare et al. 2014). Hence, it appears that magnetite from BIFs is characterized by lower overall abundances of the compatible trace elements relative to high-temperature hydrothermal magnetite (e.g., Angerer et al. 2012, Nadoll et al. 2014, Dare et al. 2014, Chen et al. 2015). In contrast to these elements, similar or higher normalized values are noted for Pb, Zr, Hf, Mn, Mo, Nb, and Cu, which might be attributable to the high solubility of Pb and contamination from ubiquitous micro- to nanometer scale inclusions (Duparc 2014) such as zircon, various sulfides, and Nb-bearing oxide grains in the magnetite layers.

Discussion

It is now widely accepted that abundance of REE + Y and the MUQ-normalized patterns of chert bands from Algoma-type BIFs may reflect primary geochemical signatures inherited through precipitation from a mixed reservoir of seawater and moderate-temperature hydrothermal vent fluids with variable amounts of detrital contamination (e.g., Bau & Dulski 1996, Thurston et al. 2012, Gourcerol et al. 2015a, b, c). Below, we assess the validity of this chemical pattern, which is also present in the magnetite layers interbedded with the cherts. using the data from the three Archean Algoma-type BIFs examined in this study. In addition, these data are then used to assess the validity of the currently defined fields for magnetite from BIF in magnetite classification diagrams (e.g., Dupuis & Beaudoin 2011, Dare et al. 2014).

Assessing the primary geochemical signature for magnetite layers

Comparison of the REE + Y distribution patterns of metalliferous sediments (on a carbonate-free basis) composed mainly of poorly crystalline to amorphous Fe-Mn oxyhydroxides and variable amorphous silicate phases from the Pacific Ocean (Fig. 6; Barrett & Jarvis 1987, Dekov et al. 2010) and the magnetite layers in this study highlights that, other than the differences in the Ce anomalies between modern metalliferous

---

Fig. 2. (continued) BSE image from the SEM of sample AMB-126242 showing magnetite bands associated with minor inclusions of quartz and apatite. (E) BSE image from the SEM showing the trace of the laser ablation traverse used for LA ICP-MS analysis in thick section of sample AMB-126249. (F) BSE image from the SEM showing the laser ablation line traverse used for LA ICP-MS analysis in thick section of sample MEL-025. AMB-XXXXXX refers to samples from Meadowbank deposit whereas MEL-XXX refers to Meliadine gold district. Abbreviations are: Ap = Apatite, Chl = Chlorite, Mt = Magnetite, Qtz = Quartz.

//titan/production/c/cami/live_jobs/cami-54/cami-54-03/cami-54-03-11/layouts/cami-54-03-11.3d
■ 4 January 2017 ■ 10:29 am ■ Allen Press, Inc.

Page 7

TABLE 1. ABUNDANCES OF ELEMENTS AND REE + Y FOR MAGNETITE SAMPLES FROM MEADOWBANK

Samples	AMB126225_M	AMB126227_M	AMB126235_M	AMB126242_M	AMB126245_M	AMB126249_M	AMB128328_M
Si (ppm)	9450	9120	16400	4800	25200	7220	14230
Li	0.235	0.151	<0.011	0.141	0.149	1.556	0.116
Be	0.436	0.649	0.281	0.596	0.504	0.505	0.354
Sc	0.461	0.275	0.235	0.591	0.741	0.332	0.212
Ti	537.000	85.300	20.280	44.850	18.350	51.500	40.280
V	13.970	6.776	2.610	5.893	1.989	2.511	4.534
Cr	21.400	8.070	4.850	4.741	8.600	4.193	7.210
Mn	41.000	57.200	8.490	76.200	646.000	30.770	5.300
Fe	99610	57200	39820	43090	113600	77860	94470
Co	0.444	0.924	0.302	1.186	5.470	0.595	0.201
Ni	12.290	2.787	6.120	1.331	3.030	0.915	0.884
Cu	1.160	1.270	1.520	0.820	1.010	2.000	0.992
Zn	11.000	5.300	2.050	5.100	5.890	6.510	2.050
Ga	1.906	1.398	0.700	0.622	3.569	1.472	1.054
As	0.252	0.394	0.191	0.790	0.472	0.856	0.199
Rb	0.617	1.690	0.162	0.149	0.108	0.260	0.367
Sr	4.320	9.260	25.600	57.800	1.940	9.080	8.190
Y	1.198	0.929	5.230	20.440	2.550	4.340	4.590
Zr	5.400	3.090	0.910	3.500	2.130	8.720	0.349
Nb	0.476	0.162	0.051	0.224	0.157	0.178	0.185
Mo	0.025	0.025	0.025	0.860	0.044	0.049	0.121
Ag	0.012	0.008	0.007	0.012	0.008	0.016	0.008
Cd	<0.71	0.154	<0.71	<0.71	<0.71	<0.71	<0.71
In	0.007	0.027	0.007	0.005	0.015	0.011	0.008
Sn	0.830	3.820	0.410	0.113	0.520	0.350	0.601
Sb	0.612	0.380	0.147	0.202	0.828	0.346	0.094
Cs	0.142	0.404	0.059	0.033	0.024	0.033	0.127
Ba	2.563	4.800	1.479	2.299	3.490	5.355	4.094
La	0.173	0.179	0.403	3.030	0.821	0.820	0.289
Ce	0.320	0.339	1.030	8.030	1.100	1.500	0.550
Pr	0.038	0.041	0.181	1.284	0.113	0.201	0.089
Sm	0.050	0.061	0.402	2.635	0.132	0.350	0.233
Eu	0.028	0.038	0.378	2.028	0.104	0.194	0.204
Gd	0.093	0.089	0.549	3.480	0.257	0.576	0.474
Tb	0.019	0.017	0.078	0.507	0.042	0.083	0.072
Dy	0.151	0.133	0.530	3.340	0.283	0.582	0.505
Ho	0.036	0.031	0.119	0.661	0.059	0.114	0.115

TABLE 1. CONTINUED

Samples	AMB126225_M	AMB126227_M	AMB126235_M	AMB126242_M	AMB126245_M	AMB126249_M	AMB128328_M
Er	0.120	0.106	0.346	1.822	0.184	0.329	0.334
Tm	0.019	0.017	0.043	0.236	0.026	0.048	0.044
Yb	0.126	0.119	0.257	1.446	0.165	0.301	0.236
Lu	0.022	0.019	0.039	0.200	0.031	0.049	0.036
Hf	0.130	0.046	0.017	0.066	0.049	0.180	<0.011
Ta	0.045	0.012	0.003	0.007	0.008	0.010	0.007
W	0.678	0.494	0.176	0.381	0.205	0.420	0.186
Au	0.011	0.011	0.011	0.011	0.011	0.011	0.000
Tl	0.008	0.016	0.006	0.003	0.005	0.004	0.006
Pb	0.927	1.750	0.360	0.865	0.550	1.490	0.343
Th	0.081	0.026	0.014	0.128	0.017	0.062	0.013
U	0.067	0.065	0.020	0.145	0.068	0.096	0.012
Y/Ho	33.094	29.586	43.950	30.923	43.220	38.171	39.775
La/La*$_{MUQ}$	1.426	1.700	1.677	1.521	2.691	2.014	2.295
Y/Y*$_{MUQ}$	1.149	1.014	1.632	1.180	1.548	1.421	1.480
Eu/Eu*$_{MUQ}$	1.764	2.166	3.752	3.138	2.649	2.064	2.984
Ce/Ce*$_{MUQ}$	1.097	1.208	1.151	1.170	1.381	1.222	1.213
Eu/Sm	0.562	0.619	0.940	0.770	0.788	0.554	0.876
Sm/Yb	0.398	0.511	1.564	1.822	0.800	1.163	0.987
(Nd/Yb)$_{MUQ}$	0.118	0.148	0.426	0.497	0.290	0.327	0.220

TABLE 2. ABUNDANCES OF ELEMENTS AND REE + Y FOR MAGNETITE SAMPLES FROM MELIADINE

Samples	MEL022_M	MEL023_M	MEL025_M	MEL028_M	MEL031_M	MEL032_M	MEL033_M	MEL034_M
Si (ppm)	55100	28100	8600	22500	38000	46200	31500	22400
Li	0.287	0.914	0.286	0.173	0.611	0.523	0.522	0.052
Be	0.081	0.040	< 0.028	0.069	0.078	0.039	0.046	0.061
Sc	1.319	0.799	0.330	0.578	0.668	1.140	0.849	0.286
Ti	27.190	32.190	79.530	49.690	46.780	78.400	61.200	46.400
V	1.404	1.443	4.375	2.710	2.847	7.790	2.156	1.752
Cr	16.140	28.900	12.920	10.850	7.260	21.000	7.330	8.860
Mn	196	109.3000	38.1000	76.7000	49.4000	71.2000	121	7.3000
Fe	83500	128500	112350	110200	93550	97200	92000	117000
Co	0.370	1.130	0.650	0.246	0.402	0.539	0.156	0.271
Ni	0.607	0.830	1.948	0.760	0.770	1.670	1.096	0.560
Cu	2.230	2.640	3.610	1.130	2.020	3.800	1.290	1.530
Zn	16.490	16.500	11.510	8.240	10.260	19.100	16.360	9.300
Ga	1.825	5.547	4.192	1.291	1.588	1.677	2.021	2.972
As	1.970	6.170	4.300	1.840	18.000	17.600	15.800	14.300
Rb	0.244	0.283	0.543	0.072	0.560	1.240	0.178	0.243
Sr	1.980	1.900	5.170	8.800	8.300	12.600	30.600	23.500
Y	2.670	1.348	0.860	1.151	0.461	2.050	5.870	1.000
Zr	2.270	2.110	3.080	0.444	1.640	2.610	11.500	0.973
Nb	0.306	1.215	0.516	0.187	0.107	0.242	0.205	0.164
Mo	0.803	0.236	0.079	0.072	0.200	0.184	0.052	0.065
Ag	0.019	0.075	0.008	0.009	0.228	0.148	0.050	0.037
Cd	0.146	0.060	0.041	0.063	0.462	0.396	0.219	0.170
In	0.007	0.013	0.011	0.006	0.030	0.016	0.018	0.015
Sn	0.147	0.126	0.139	0.142	0.173	0.239	0.079	0.077
Sb	0.206	0.189	0.153	0.195	0.321	0.193	0.068	0.050
Cs	0.107	0.125	0.110	0.023	0.151	0.251	0.028	0.062
Ba	2.836	2.880	3.160	2.015	3.610	1.183	0.725	0.341
La	0.163	0.730	0.221	0.216	0.077	1.310	15.000	0.080
Ce	0.383	1.830	0.660	0.399	0.175	4.100	26.000	0.258
Pr	0.049	0.224	0.083	0.053	0.027	0.490	2.800	0.039
Nd	0.254	0.950	0.440	0.269	0.134	1.960	11.000	0.231
Sm	0.100	0.289	0.142	0.082	0.049	0.430	1.500	0.090
Eu	0.029	0.061	0.040	0.025	0.019	0.144	0.540	0.049
Gd	0.202	0.252	0.109	0.111	0.064	0.460	1.180	0.152
Tb	0.042	0.040	0.017	0.019	0.011	0.063	0.143	0.023
Dy	0.350	0.265	0.131	0.147	0.081	0.342	0.960	0.153

TABLE 2. CONTINUED

Samples	MEL022_M	MEL023_M	MEL025_M	MEL028_M	MEL031_M	MEL032_M	MEL033_M	MEL034_M
Ho	0.082	0.047	0.028	0.033	0.019	0.060	0.187	0.032
Er	0.268	0.153	0.075	0.116	0.056	0.164	0.561	0.087
Tm	0.039	0.023	0.010	0.017	0.010	0.021	0.079	0.011
Yb	0.268	0.139	0.061	0.121	0.070	0.128	0.517	0.054
Lu	0.044	0.021	0.009	0.020	0.013	0.020	0.078	0.009
Hf	0.041	0.048	0.039	<0.009	0.031	0.053	0.318	0.019
Ta	0.005	0.026	0.044	0.006	0.007	0.011	0.016	0.011
W	0.102	0.151	0.070	0.128	0.242	0.131	0.075	0.126
Au	0.030	1.600	0.005	0.027	0.460	0.270	0.204	0.166
Tl	0.010	0.013	0.007	0.006	0.024	0.027	0.007	0.012
Pb	0.925	0.599	0.255	0.288	0.834	1.000	0.770	0.331
Th	0.055	0.118	0.180	0.012	0.047	0.215	3.100	0.019
U	0.048	0.180	0.069	0.017	0.036	0.065	0.414	0.043
Y/Ho	32.561	28.439	30.389	34.985	24.785	34.167	31.390	30.568
La/La*$_{MUQ}$	1.548	1.021	1.304	1.799	1.210	0.745	1.441	1.449
Y/Y*$_{MUQ}$	1.137	1.000	1.182	1.173	0.907	1.309	1.147	1.200
Eu/Eu*$_{MUQ}$	0.895	0.932	1.285	1.128	1.429	1.467	1.840	1.675
Ce/Ce*$_{MUQ}$	1.241	1.066	1.297	1.162	0.982	1.030	1.122	1.171
Eu/Sm	0.293	0.210	0.280	0.304	0.383	0.335	0.360	0.449
Sm/Yb	0.374	2.087	2.320	0.675	0.696	3.359	2.901	1.879
(Nd/Yb)$_{MUQ}$	0.087	0.631	0.661	0.204	0.176	1.408	1.956	0.340

TABLE 3. ABUNDANCES OF ELEMENTS AND REE + Y FOR MAGNETITE SAMPLES FROM MUSSELWHITE

Samples	E599661_M	E599668_M	E599671_M
Si (ppm)	51670	48700	34000
Li (ppm)	0.553	0.111	0.771
Be (ppm)	0.182	0.620	0.429
Sc (ppm)	2.258	0.440	0.340
Ti (ppm)	315.400	8.190	8.490
V (ppm)	40.290	3.541	2.358
Cr (ppm)	8.290	9.550	13.600
Mn (ppm)	2602	372	240
Fe (ppm)	79000	116700	88200
Co (ppm)	3.377	0.978	0.850
Ni (ppm)	5.830	1.624	1.021
Cu (ppm)	1.350	3.720	1.120
Zn (ppm)	16.440	9.300	7.450
Ga (ppm)	5.170	1.195	0.495
As (ppm)	0.692	0.281	0.605
Rb (ppm)	8.660	1.066	0.430
Sr (ppm)	3.350	13.760	1.530
Y (ppm)	1.217	5.310	5.010
Zr (ppm)	2.270	0.154	0.048
Nb (ppm)	0.318	0.240	0.123
Mo (ppm)	0.084	0.062	0.010
Ag (ppm)	0.012	0.021	0.004
Cd (ppm)	<0.071	0.187	<0.071
In (ppm)	0.021	0.013	0.009
Sn (ppm)	0.203	0.177	0.136
Sb (ppm)	0.277	0.298	0.502
Cs (ppm)	0.759	0.382	0.150
Ba (ppm)	34.100	2.811	2.150
La (ppm)	0.267	0.843	0.750
Ce (ppm)	0.469	1.926	2.190
Pr (ppm)	0.063	0.284	0.338
Nd (ppm)	0.366	1.505	1.840
Sm (ppm)	0.134	0.419	0.482
Eu (ppm)	0.072	0.306	0.305
Gd (ppm)	0.190	0.553	0.598
Tb (ppm)	0.026	0.086	0.085
Dy (ppm)	0.150	0.658	0.604
Ho (ppm)	0.029	0.148	0.140
Er (ppm)	0.079	0.467	0.468
Tm (ppm)	0.011	0.070	0.073
Yb (ppm)	0.078	0.465	0.529
Lu (ppm)	0.015	0.075	0.087
Hf (ppm)	0.053	<0.011	<0.011
Ta (ppm)	0.019	0.003	0.003
W (ppm)	0.501	0.232	0.182
Au (ppm)	<0.015	<0.015	<0.015
Tl (ppm)	0.032	0.011	0.003
Pb (ppm)	0.708	1.355	0.570
Th (ppm)	0.112	0.007	0.007
U (ppm)	0.092	0.009	0.009
Y/Ho	41.395	35.806	35.786
La/La*$_{MUQ}$	2.457	1.452	1.146

TABLE 3. CONTINUED

Samples	E599661_M	E599668_M	E599671_M
Y/Y*$_{MUQ}$	1.604	1.276	1.234
Eu/Eu*$_{MUQ}$	2.117	2.859	2.615
Ce/Ce*$_{MUQ}$	1.318	1.105	1.085
Eu/Sm	0.535	0.730	0.633
Sm/Yb	1.709	0.901	0.911
(Nd/Yb)$_{MUQ}$	0.429	0.298	0.320

sediments *versus* Archean BIFs, which is due to oxidation of Ce^{3+} to Ce^{4+} in the oxic water column, the REE + Y distribution patterns of these two sample suites are very similar. In addition, both modern metalliferous sediments and ancient magnetite layers in BIFs show depletion in LREE relative to middle and HREE with associated slight to moderate positive La, Y, and Eu anomalies. It is widely accepted that the depletion in LREE relative to HREE with associated variable positive La and Y anomalies represents fractionation of the REE and Y in an ambient seawater column due to the preferential removal of these elements onto Fe-oxyhydroxides, organic matter, and clay particles (*e.g.*, Bau & Dulski 1996, Thurston *et al.* 2012, Gourcerol *et al.* 2015a, b, c). Furthermore, a positive Eu anomaly is a common feature in rocks considered to have precipitated from Archaean seawater modified by moderate-temperature (*i.e.*, >250 °C) hydrothermal or vent-sourced fluids (*e.g.*, Bau & Dulski 1996, Kamber *et al.* 2004). We note that these aforementioned features are present even though the magnetite layers record some contamination, as indicated by high Si concentrations (Fig. 4) (due to primary chert and detrital quartz or silicates) which have partly diluted the primary geochemical signature. However, as the Si concentration is around 10% of the Fe concentration, it is unlikely that the primary signature in oxide layers may be completely dissolved.

We conclude based on the data presented that the analyzed magnetites record a primary geochemical signature that reflects the influence of ambient seawater and a variable input of moderate-temperature (> 250 °C) hydrothermal vent fluids (Figs. 1, 2) during Fe-oxyhydroxide deposition, despite the overprinting effects of later diagenetic processes and later meta-morphic or hydrothermal events suggested by petro-graphic observations (*e.g.*, various magnetite events). Additionally, the chondritic Y/Ho ratios associated with high REE content may be indicative of variable detrital contamination with the positive Ce anomalies observed in most of the samples reflecting precipita-tion of primary Fe-oxyhydroxide at pH values <5, as suggested in Gourcerol *et al.* (2015b). The chondritic Y/Ho ratios would also indicate that the hydrothermal
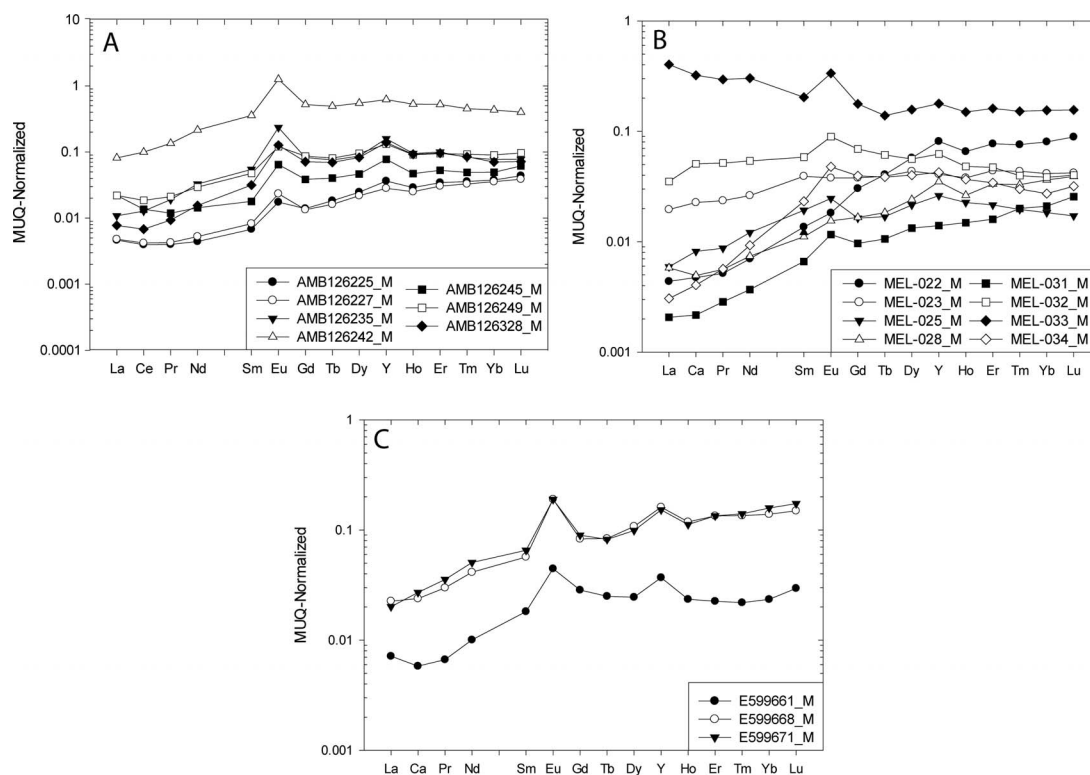
Fig. 3. Shale (MUQ) – normalized REE distribution patterns for magnetite layers sampled from the (A) Meadowbank, (B) Meliadine, and (C) Musselwhite BIF-hosted gold deposits.

fluids did not contain significant F and Cl which would serve to fractionate Y and Ho (Loges *et al.* 2013).

Magnetites from all three deposits have similar REE + Y characteristics, which indicate that the gold mineralizing process has not altered the primary geochemistry of the magnetite layers in the iron formations. Given that the REE + Y signatures of the magnetite layers are similar to the REE + Y signatures of the chert bands, we can state that the primary geochemical signature of the iron formation as a whole is preserved in spite of subsequent diagenetic and metamorphic/hydrothermal processes. Establishing any further effects of low temperature diagenesis will require *in situ* O isotopic research.

Assessing and comparing the primary geochemical signatures between chert and magnetite layers

Based on the above discussion of the magnetite layers and our previous work on the adjacent chert bands (Gourcerol *et al.* 2015a, b), a reasonable case is made here that these two data sets record the primary geochemical signal of the ocean water column at the time of their initial formation as Fe- and Si-rich

chemical precipitates, respectively. In order to compare and contrast the signals present in these layers, the data are compared in Figure 7, where a binary mixing line was calculated using seawater and hydrothermal vent fluids as endmembers. This diagram allows us to: (1) explore the relative influence of these endmember components during precipitation of the primary Fe-oxyhydroxide material and (2) evaluate the variation between chert and magnetite regarding their primary geochemical signatures. The two endmembers of the mixing line represented in Figure 7 are: (1) modern seawater composition from the North Pacific (Alibo & Nozaki 1999) and (2) an Archean hydrothermally precipitated chert from the Abitibi greenstone belt (*i.e.*, 06PCT001M; Thurston *et al.* 2012). The selection of the latter chert sample is explained in detail by Gourcerol *et al.* (2015b).

Most of the samples in this study fall on the mixing line despite the fact that some of the samples analyzed exhibit high Sm/Yb ratios (Fig. 7). The Sm/Yb ratio is particularly sensitive to the presence of high-pressure metamorphic phases that may be present in the samples as contaminants, such as amphibole and
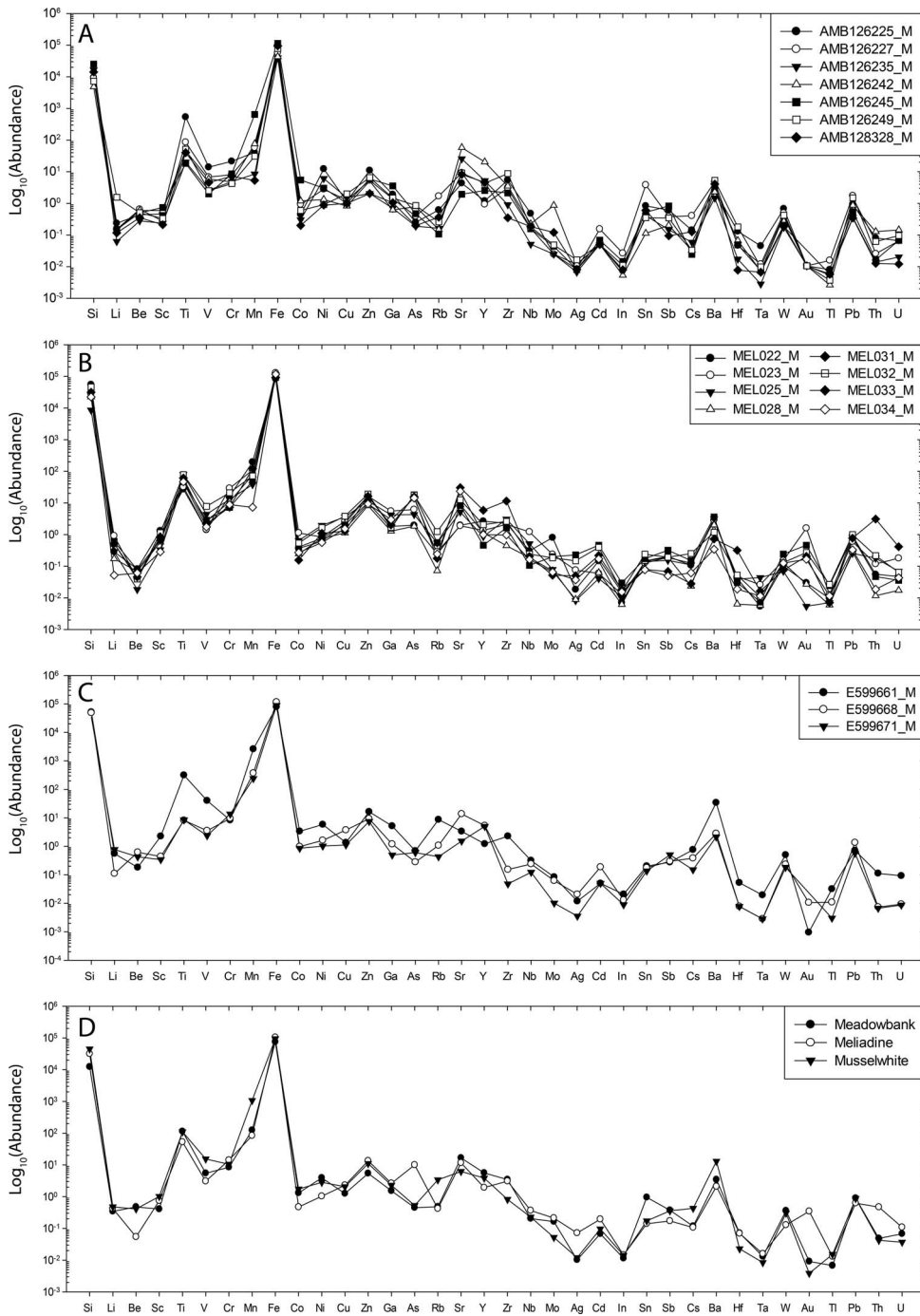
Fig. 4. Spider-type plots that summarize the abundances of major and trace elements for magnetite layers from the (A) Meadowbank, (B) Meliadine, and (C) Musselwhite BIF-hosted gold deposits and (D) the average of each deposit.
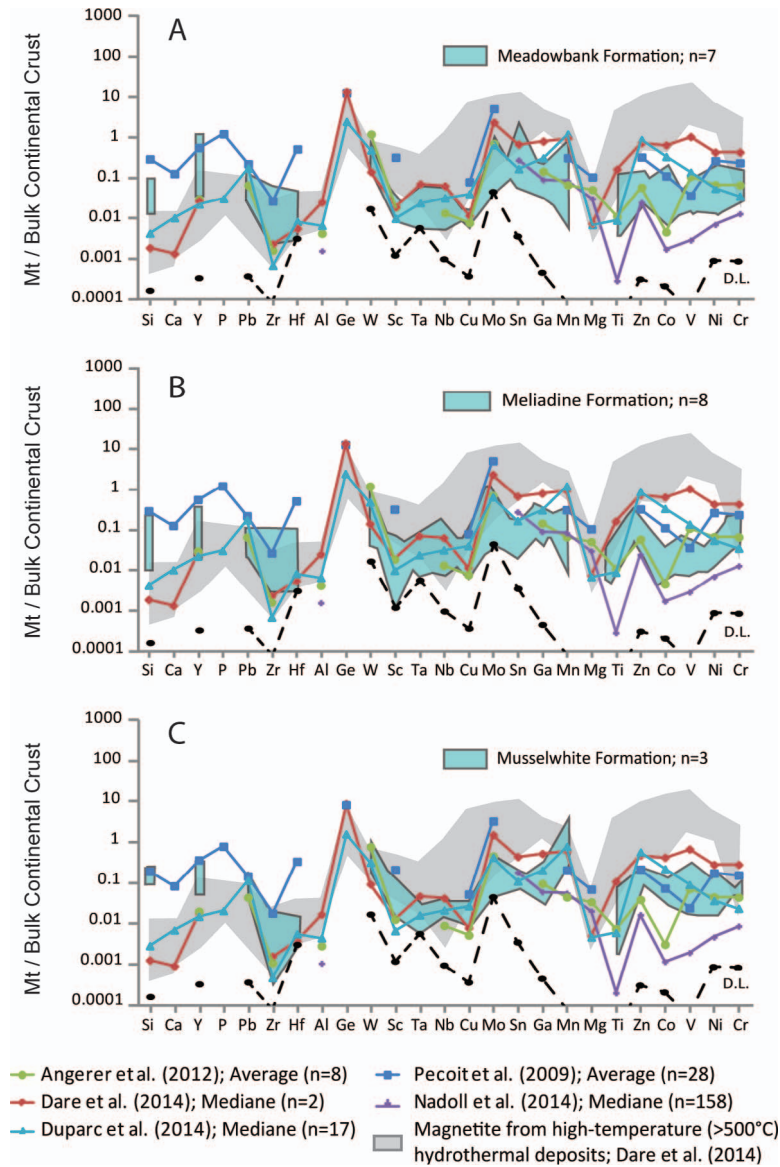
FIG. 5. Multi-element extended spider diagrams (after Dare *et al.* 2014) for various analyses of magnetite normalized to bulk continental crust (values from Rudnick & Gao 2003). The plots show a comparison of magnetite samples from the (A) Meadowbank, (B) Meliadine, and (C) Musselwhite BIF-hosted gold deposits with data for both whole rock (Pecoits *et al.* 2009, Angerer *et al.* 2012) and *in situ* (Dare *et al.* 2014, ~~Dupuis *et al.* 2014,~~ Nadoll *et al.* 2014) analyses of magnetites from BIFs in the literature. For comparison, the patterns for samples of low-temperature BIF magnetite in the BIFs of this study (in blue) are seen to contrast with the field (in grey) for high-temperature hydrothermal magnetites (from Dare *et al.* 2014). The detection limit for the data in this study is illustrated by the dashed black line entitled D.L.

garnet, which may overprint the primary geochemical signature of the BIFs. We note that the Sm/Yb ratios are, relatively speaking, a bit higher for magnetite samples (Fig. 7A) than for adjacent chert samples (Fig. 7B). The variable input of the moderate-temperature hydrothermal vent fluid displayed in Figure 7A suggests a contribution of less than 10%, which is very similar to the corresponding chert layers which

//titan/production/c/cami/live_jobs/cami-54/cami-54-03/cami-54-03-11/layouts/cami-54-03-11.3d
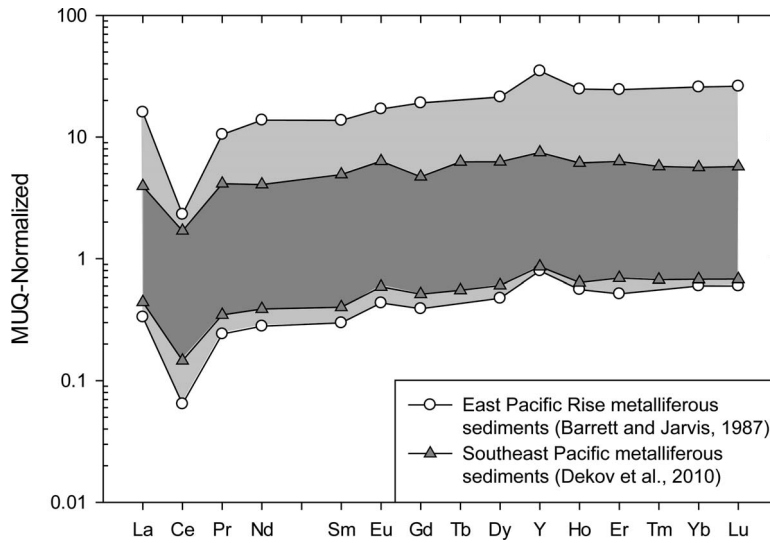■ 4 January 2017 ■ 10:29 am ■ Allen Press, Inc.

Page 15

FIG. 6. Shale (MUQ) – normalized REE distribution patterns for metalliferous sediments (on a carbonate-free basis) from the East Pacific Rise (light grey: Barrett & Jarvis 1987) and from the southeast Pacific (dark grey: Dekov *et al.* 2010). These metalliferous sediments are composed of poorly crystalline to X-ray amorphous Fe-Mn oxyhydroxides and variable amounts of amorphous silicate phases.
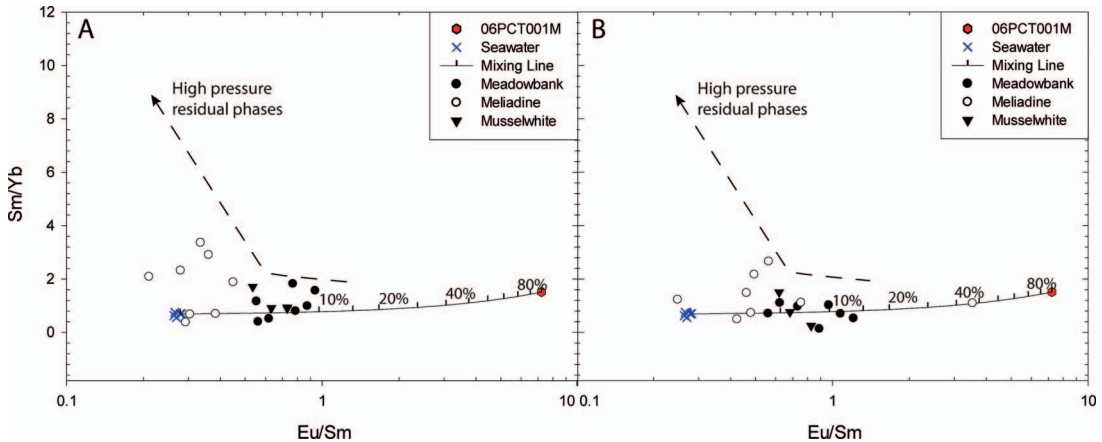

FIG. 7. Binary plots of elemental ratio data (Eu/Sm and Sm/Yb) for magnetite samples (A) and corresponding chert samples (B) from the Meadowbank, Meliadine, and Musselwhite BIF-hosted gold deposits. This type of plot is used to assess the potential influence of high-*T* hydrothermal fluids on the chemistry of iron oxides *versus* low-*T* fluids (*i.e.*, ambient seawater). The data for the high-*T* hydrothermal fluid, represented by 06PCT001M, is from Thurston *et al.* (2012) whereas the data for seawater is from Alibo & Nozaki (1999).

record a hydrothermal fluid contribution of between 0 and 15%, excluding one sample that records 46% (Fig. 7B). These observations confirm the influence of moderate-temperature hydrothermal fluids during Fe-oxyhydroxide precipitation, but also that magnetite can be used as well as chert bands to assess the origin of BIFs.

Assessment of discriminant diagrams for magnetite layers

The advent of modern analytical methods, such as LA-ICP-MS, has provided a means to assess the use of discriminant diagrams based on the chemistry of magnetite to define fields for different ore deposit
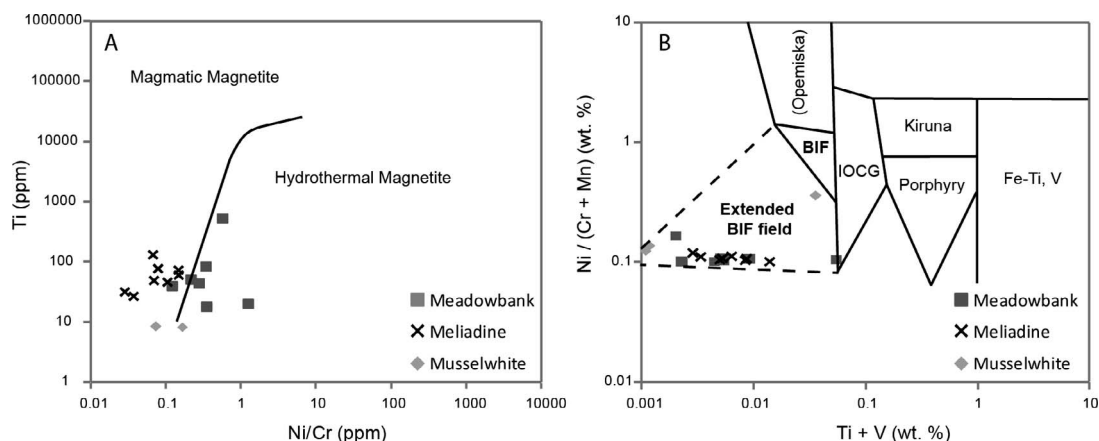
FIG. 8. Genetic classification diagrams for magnetite from a variety of ore deposit settings. (A) The Ti (ppm) *versus* Ni/Cr ratio (un-normalized) diagram of Dare *et al*. (2014) that is used to discriminate magnetite from magmatic and hydrothermal settings. It is noted that two samples of the Musselwhite deposit are superimposed to each other explaining why there is only two visible points. (B) The Ni/(Cr + Mn) *versus* Ti + V discriminant diagram of Dupuis & Beaudoin (2011) that is used to discriminate magnetite in a variety of ore deposit types: BIF, Kiruna apatite-magnetite, iron-oxide-copper-gold (IOCG), porphyry Cu, magmatic Fe-Ti-V oxide, and Opemiska-type Cu veins. A new extended BIF field associated with dashed black lines is proposed for this diagram according to the studied samples.

types due to its occurrence in a wide variety of environments (Dupuis & Beaudoin 2011). This classification scheme also includes chemical space for samples from BIF, but the defined area is controversial, as magnetite layers from Algoma-type BIF do not correspond to the simple binary magmatic or hydrothermal sources, but rather reflect interaction of hydrothermal vent fluids with seawater (*i.e.*, hydrogeneous origin). According to Nadoll *et al*. (2014), the composition of magnetite from BIFs is mainly controlled by the chemistry of the ocean water column and its related reservoirs (*i.e.*, seawater *versus* vent fluid) and temperature and $f\mathrm{O_2}$. In addition, the substrate may also be important in terms of determining some elemental components of the magnetite chemical signature obtained *via* leaching of the underlying rock by the vent fluids, which may be reflected in the relative enrichment in Sc, Mn, Ti, Zn, and Cr (Pecoits *et al*. 2009, Dare *et al*. 2014). In regards to the relative enrichment of Ti in magnetite samples, this may be related to the influence of higher fluid temperatures (*e.g*., Thorne *et al*. 2008, Nadoll *et al*. 2014).

Using the data from this study, it may be possible to evaluate the proposed classification diagrams with regard to BIFs, as shown with the relevant diagrams in Figure 8. In the Ti *versus* Ni/Cr diagram of Dare *et al*. (2014), 60% of our samples plot in the magmatic field with the remainder falling in the hydrothermal field

(Fig. 8A). We propose that the distribution of the data in this plot may illustrate a combination of a moderate-temperature hydrothermal influence (>250 °C) and variable leaching of magnetite-bearing mafic/ultramafic rocks by hydrothermal fluids, as most of the samples in this study are located close to the boundary line of the two magmatic and hydrothermal fields. This hypothesis is also supported by the fact that Ni and Cr are decoupled, probably due to the higher solubility of Ni compared to Cr in the hydrothermal fluids (Dare *et al*. 2014). Moreover, as magnetite layers may reflect the earlier precipitation of Fe-oxyhydroxides, trace elements which show a good to moderate correlation with Fe may reflect the water-column geochemistry of the environment in which they were precipitated (either from hydrothermal fluids or weathering of basement or detrital contamination) and in which they were scavenged by adsorption onto Fe-oxyhydroxide surface. However, we conclude that this diagram should be used with caution regarding provenance or source discrimination for a given magnetite.

As for the Ni/(Cr + Mn) *versus* Ti + V diagram of Dupuis & Beaudoin (2011), the samples do not plot in the expected BIF field, as defined by several previous studies (*e.g*., Duparc *et al*. 2015, Nadoll *et al*. 2014, Chen *et al*. 2015; Fig. 8B), and instead depart markedly in regard to both of the chemical parameters used. These findings are consistent with the more recent studies which also indicate that these classifi-

//titan/production/c/cami/live_jobs/cami-54/cami-54-03/cami-54-03-11/layouts/cami-54-03-11.3d
■ 4 January 2017 ■ 10:29 am ■ Allen Press, Inc.

Page 17

cation schemes are not always reliable in correctly classifying magnetite from low- to moderate-temperature hydrothermal deposits or BIF (Hu *et al.* 2014, Chen *et al.* 2015, Zhao & Zhou, 2015) and, therefore, indicates that such plots need to be used with caution with regards to Algoma-type BIF. We suggest an extended BIF field based on our samples illustrated by dashed lines in Figure 8.

Conclusions

This LA-ICP-MS study of the trace element chemistry of magnetite from BIF-hosted gold deposit settings, in particular the REE + Y systematics, suggests that despite the potential influence of diagenetic processes or later stage metamorphism, and interaction with hydrothermal fluids and mineralizing events on the original Fe-oxide material, the magnetite layers apparently retain their primary geochemical signature (*e.g.*, seawater and moderate-temperature hydrothermal vent fluids). This latter hypothesis is validated by the fact that the same conclusions were previously determined in a similar LA-ICP-MS trace element study of adjacent chert layers from the same material. Furthermore, these data, in conjunction with appropriate binary mixing diagrams, provide a means to evaluate the proportional contributions of the two endmember fluids involved in formation of BIF material, both the chert and magnetite layers. The additional chemical data obtained in this study have been used to examine the current use of discriminant diagrams for distinguishing magmatic *versus* hydrothermal magnetite and also to which ore deposit type the magnetite chemistry shows the closest affinity. Based on the data for these samples, we would caution using such diagrams for at least BIF samples, although we note that some of the problems encountered may also be relevant to other hydrothermal type settings.

Acknowledgments

References

Alibo, D.S. & Nozaki, Y. (1999) Rare earth elements in seawater: particle association, shale-normalization, and Ce oxidation. *Geochimica et Cosmochimica Acta* **63**, 363–372.

Allwood, A.C., Kamber, B.S., Walter, M.R., Burch, I.W., & Kanik, I. (2010) Trace element record depositional history of an Early Archean stromatolitic carbonate platform. *Chemical Geology* **270**, 148–163.

Angerer, T., Hagemann, S.G., & Danyushevsky, L. (2012) Geochemical evolutions of the banded iron formation-hosted high-grade iron ore system in the Koolyanobbing Greenstone Belt, Western Australia. *Economic Geology* **107**, 599–644.

Armitage, A.E., James, R.S., & Goff, S.P. (1996) Gold mineralization in Archean banded iron formation, Third Portage Lake area, Northwest Territories, Canada. *Exploration and Mining Geology* **5(1)**, 1–15.

Aspler, L.B. & Chiarenzelli, J.R. (1996a) Stratigraphy, sedimentology and physical volcanology of the Henik Group, central Ennadai-Rankin greenstone belt, Northwest Territories, Canada: Late Archean paleogeography of the Hearne Province and tectonic implications. *Precambrian Research* **77**, 59–89.

Barrett, T.J. & Jarvis, I. (1988) Rare-earth-element geochemistry of metalliferous sediments from DSDP LEG 92: The East Pacific Rise Transect. *Chemical Geology* **67**, 243–259.

Bau, M. & Dulski, P. (1996) Distribution of Y and rare-earth elements in the Penge and Kuruman Iron Formations, Transvaal Supergroup, South Africa. *Precambrian Research* **79**, 37–55.

Biczok, J., Hollings, P., Klipfel, P., Heaman, L., Maas, R., Hamilton, M., Kamo, S., & Friedman, R. (2012) Geochronology of the North Caribou greenstone belt, Superior Province Canada: Implications for tectonic history and gold mineralization at the Musselwhite mine. *Precambrian Research* **192–195**, 209–230.

Bolhar, R., Van Kranendonk, M.J., & Kamber, B.S. (2005) A trace element study of siderite-jasper banded iron formation in the 3.45 Ga Warrawoona Group, Pilbara craton-Formation from hydrothermal fluids and shallow seawater. *Precambrian Research* **137**, 93–114.

Breaks, F.W., Osmani, I.A., & DeKemp, E.A. (2001) Geology of the North Caribou Lake area, northwestern Ontario. Ontario Geological Survey, Open File Report **6023**, 80 pp.

Carpenter, R.L. (2004) *Relative and absolute timing of supracrustal deposition, tectonothermal activity and gold mineralization, West Meliadine region, Rankin Inlet greenstone belt, Nunavut, Canada.* Ph.D. Thesis, Faculty of Graduate Studies, University of Western Ontario, London, Ontario, Canada, 362 pp.

CARPENTER, R.L., DUKE, N.A., SANDEMAN, H.A., & STERN, R. (2005) Relative and absolute timing of gold mineralization along the Meliadine Trend, Nunavut, Canada; evidence for Paleoproterozoic gold hosted in an Archean greenstone belt. *Economic Geology and the Bulletin of the Society of Economic Geologists* **100**, 567–576.

CHEN, W.T., ZHOU, M.-F., LI, X., GAO, J.F., & HOU, K. (2015) *In-situ* LA-ICP-MS trace elemental analyses of magnetite: Cu-(Au, Fe) deposits in the Khetri copper belt in Rajasthan Province, NW India. *Ore Geology Reviews* **65**, 929–939.

DARE, S.A.S., BARNES, S.J., & BEAUDOIN, G. (2012) Variation in trace element content of magnetite crystallized from a fractionating sulfide liquid, Sudbury, Canada: Implications for provenance discrimination. *Geochimica et Cosmochimica Acta* **88**, 27–50.

DARE, S.A.S., BEAUDOIN, G., MÉRIC, J., BOUTROY, E., & POTVIN-DOUCET, C. (2014) Trace elements in magnetite as petrogenetic indicators. *Mineralium Deposita* **49(7)**, 785–796.

DAVIS, W.J., RYAN, J.J., SANDEMAN, H.A., & TELLA, S. (2008) A Paleoproterozoic detrital zircon age for a key conglomeratic horizon within the Rankin Inlet area, Kivalliq region, Nunavut: implications for Archean and Proterozoic evolution of the area. Geological Survey of Canada, Current research 2008-8, 10 pp.

DEKOV, V.M., CUADROS, J., KAMENOV, G.D., WEISS, D., ARNOLD, T., BASAK, C., & ROCHETTE, R. (2010) Metalliferous sediments from the H.M.S. Challenger voyage (1872–1876). *Geochemica et Cosmochimica Acta* **74**, 5019–5038.

DUPARC, Q. (2014) *Corrélations de formations sédimentaires du nord-est de la sous-province de La Grande, Québec, Canada*. Unpublished Master's Thesis, Université du Québec à Chicoutimi, 243 pp.

DUPARC, Q., DARE, S.A.S., COUSINEAU, P.A., & GOUTIER, J. (2015) Magnetite chemistry as a provenance indicator in Archean metamorphosed sedimentary rocks. *Journal of Sedimentary Research* (accepted).

DUPUIS, C. & BEAUDOIN, G. (2011) Discriminant diagrams for iron oxide trace element fingerprinting of mineral deposit types. *Mineralium Deposita* **46**, 319–335.

GOURCEROL, B., THURSTON, P.C., KONTAK, D.J., & CÔTÉ-MANTHA, O. (2015a) The geochemistry of chert from the Banded Iron Formation-type Musselwhite and Meadowbank gold deposits: Distinguishing primary and mineralization-related signatures of chert. Geological Survey of Canada, Current research 2015-1, 24 pp.

GOURCEROL, B., THURSTON, P.C., KONTAK, D.J., CÔTÉ-MANTHA, O., & BICZOK, J. (2015b) Depositional Setting of Algoma-type Banded Iron Formation from the Meadowbank, Meliadine and Musselwhite gold deposits. *In* Targeted Geoscience Initiative 4: Contributions to the Understanding of Precambrian Lode Gold Deposits and Implications for Exploration (B. Dubé & P. Mercier-Langevin, eds.). Geological Survey of Canada, Open File **7852** (55 –68).

GOURCEROL, B., THURSTON, P.C., KONTAK, D.J., & CÔTÉ-MANTHA, O. (2015c) Interpretations and implications of preliminary LA ICP-MS analysis of chert for the origin of geochemical signatures in banded iron formations (BIFs) from the Meadowbank gold deposit, Western Churchill Province, Nunavut. *Chemical Geology* **410**, 89–107.

GRIGSBY, J. (1990) Detrital magnetite as a provenance indicator. *Journal of Sedimentary Research* **60**, 940–951.

HALL, R.S. & RIGG, D.M. (1986) Geology of the West Anticline Zone, Musselwhite Prospect, Opapimiskan Lake, Ontario, Canada. *In* Gold '86; an international symposium on the geology of gold deposits (A.J. Macdonald, ed.). Proceedings volume, GOLD '86, Toronto, Ontario, Canada, 124–136.

HRABI, R.B., BARCLAY, W.A., FLEMING, D., & ALEXANDER, R.B. (2003) Structural evolution of the Woodburn Lake group in the area of the Meadowbank gold deposit, Nunavut. Geological Survey of Canada, Current Research 2003-C27, 10 pp.

HU, H., LI, J.W., LENTZ, D., REN, Z., ZHAO, X.F., DENG, X.D., & HALL, D. (2014) Dissolution– reprecipitation process of magnetite from the Chengchao iron deposit: insights into ore genesis and implication for *in-situ* chemical analysis of magnetite. *Ore Geology Reviews* **57**, 393–405.

JANVIER, V., CASTONGUAY, S., MERCIER-LANGEVIN, P., DUBÉ, B., MCNICOLL, V., PEHRSSON, S., MALO, M., DE CHAVIGNY, B., & COTE-MANTHA, O. (2015) Preliminary results of geology of the Portage deposit, Meadowbank gold mine, Churchill Province, Nunavut, Canada. Geological Survey of Canada, Current Research 2015-2, 18 pp.

KAMBER, B.S., BOLHAR, R., & WEBB, G.E. (2004) Geochemistry of late Archean stromatolites from Zimbabwe: evidence for microbial life in restricted epicontinental seas. *Precambrian Research* **132**, 379–399.

KAMBER, B.S., GREIG, A., & COLLERSON, K.D. (2005) A new estimate for the composition of weathered young upper continental crust from alluvial sediments, Queensland, Australia. *Geochimica et Cosmochimica Acta* **69**, 1041–1058.

KAPPLER, A., PASQUERO, C., KONHAUSER, K.O., & NEWMAN, D.K. (2005) Deposition of banded iron formations by anoxygenic phototrophic Fe(II)-oxidizing bacteria. *Geology* **33**, 865–868.

KONHAUSER, O.K., NEWMAN, D.K., & KAPPLER, A. (2005) The potential significance of microbial Fe(III) reduction during deposition of Precambrian banded iron formations. *Geobiology* **3**, 167–177.

KONHAUSER, O.K., PECOITS, E., LALONDE, S.V., PAPINEAU, D., NISBET, E.G., BARLEY, M.E., ARNDT, N.T., ZAHNLE, K., &

KAMBER, B.S. (2009) Oceanic nickel depletion and a methanogen famine before the Great Oxidation Event. Nature 458, 750–753.

LAWLEY, C.J.M., DUBÉ, B., Mercier- Langevin, P., Kjarsgaard, B., Knight, R., & Vaillancourt, D. (2015) Defining and mapping hydrothermal footprints at the BIF-hosted Meliadine gold district, Nunavut, Canada. Journal of Geochemical Exploration 155, 33–55.

LAWRENCE, M.G. & KAMBER, B.S. (2006) The behavior of the rare earth elements during estuarine mixing- revisited. Marine Chemistry 100, 147–161.

LI, W., JIN, X., GAO, B., WANG, C., & ZHANG, L. (2014) Analysis of ultra-low level rare earth elements in magnetite samples from banded iron formations using HR-ICP-MS after chemical separation. Analytical Methods 6, 6125–6132.

LOGES, A., MIGDISOV, A.A., WAGNER, T., WILLIAMS-JONES, A.E., & MARKL, G. (2013) An experimental study of the aqueous solubility and speciation of Y(III) fluoride at temperatures up to 250 °C. Geochimica et Cosmochimica Acta 123, 403–415.

MCNICOLL, V., DUBÉ, B., BICZOK, J., CASTONGUAY, S., OSWALD, W., MERCIER-LANGEVIN, P., SKULSKI, T., & MALO, M. (2013) The Musselwhite gold deposit, North Caribou greenstone belt, Ontario: new high-precision U-Pb ages and their impact on the geological and structural setting of the deposit. Abstract, Geological Association of Canada Annual Meeting, Winnipeg, Canada.

MORAN, P. (2008) Lithogeochemistry of the sedimentary stratigraphy and metasomatic alteration in the Musselwhite gold deposit. North Caribou Lake metavolcanic-metasedimentary belt, Superior Province, Canada: implications for deposition and mineralization. Unpublished Master's Thesis, Lakehead University, Thunder Bay, Ontario, 351 pp.

NADOLL, P., MAUK, J.L., HAYES, T.S., KOENIG, A.E., & BOX, S.E. (2012) Geochemistry of magnetite from hydrothermal ore deposits and host rocks of the Mesoproterozoic Belt Supergroup, United States. Economic Geology 107, 1275–1292.

NADOLL, P., ANGERER, T., MAUK, J.L., FRENCH, D., & WALSHE, J. (2014) The chemistry of hydrothermal magnetite: A review. Ore Geology Reviews 61, 1–32.

OSWALD, W., CASTONGUAY, S., DUBÉ, B., MCNICOLL, V.J., BICZOK, J., MALO, M., & MERCIER-LANGEVIN, P. (2015) Geological setting of the world-class Musselwhite gold Mine, Superior Province, northwestern Ontario, and implications for exploration. In Targeted Geoscience Initiative 4: Contributions to the Understanding of Precambrian Lode Gold Deposits and Implications for Exploration (B. Dubé & P. Mercier-Langevin, eds.). Geological Survey of Canada, Open File 7852, 69–84.

PATON, C., HELLSTROM, J., PAUL, B., WOODHEAD, J., & HERGT, J. (2011) Iolite: Freeware for the visualisation and processing of mass spectrometric data. Journal of Analytical Atomic Spectrometry 26, 2508–2518.

PECOITS, E., GRINGAS, M.K., BARLEY, M.E., KAPPLER, A., POSTH, N.R., & KONHAUSER, K.O. (2009) Petrography and geochemistry of the Dales Gorge banded iron formation: Paragenetic sequence, source and implications for palaeo-ocean chemistry. Precambrian Research 172, 163–187.

PEHRSSON, S.J., WILKINSON, L., & ZALESKI, E. (2004) Geology of the Meadowbank gold deposit area, Nunavut. Geological Survey of Canada, Open File 4269, scale 1:20,000.

PEHRSSON, S.J., BERMAN, R.G., & DAVIS, W.J. (2013) Paleoproterozoic orogenesis during Nuna aggregation: a case study of reworking of the Rae craton, Woodburn Lake, Nunavut. Precambrian Research 232, 167–188.

PICKARD, A.L., BARLEY, M.E., & KRAPEZ, B. (2003) Deep-marine depositional setting of banded iron formation: sedimentological evidence from interbedded clastic sedimentary rocks in the early palaeoproterozoic Dales Gorge member of Western Australia. Sedimentary Geology 170, 37–62.

POSTH, N.R., KOHLER, I., SWANNER, E.D., SCHRODER, C., WELLMANN, E., BINDER, B., KONHAUSER, K.O., NEUMANN, U., BERTHOLD, C., NOWAK, M., & KAPPLER, A. (2013) Simulating Precambrian banded iron formation diagenesis. Chemical Geology 362, p. 66–73.

RAY, G. & WEBSTER, I. (2007) Geology and chemistry of the low Ti magnetite-bearing Heff Cu-Au skarn and its associated plutonic rocks, Heffley Lake, south-central British Columbia. Exploration and Mining Geology 16, 159–186.

RUDNICK, R.L. & GAO, S. (2003) Composition of the continental crust. In The Crust. Treatise on Geochemistry 3 (H.D. Holland & K.K. Turekian, eds.). Elsevier, Oxford, England (1–64).

SHERLOCK, R.L., ALEXANDER, R.B., MARCH, R., & BARCLAY, W.A. (2001a) Geologic setting of the Meadowbank iron formation-hosted gold deposits. Geological Survey of Canada, Current Research 2001-C11, 23 pp.

SHERLOCK, R.L., ALEXANDER, R.B., MARCH, R., & BARCLAY, W.A. (2001b) Geologic setting of the Meadowbank iron formation-hosted gold deposits. Geological Survey of Canada, Open File 3149, scale 1:10,000.

SHERLOCK, R., PEHRSSON, S., LOGAN, A.V., HRABI, R.B., & DAVIS, W.J. (2004) Geologic setting of the Meadowbank gold deposits, Woodburn Lake group, Nunavut. Exploration and Mining Geology 13(1–4), 67–107.

SHIBUYA, T., KOMIYA, T., NAKAMURA, K., TAKAI, K., & MARUYAMA, S. (2010) Highly alkaline, high-temperature hydrothermal fluids in the early Archean ocean. Precambrian Research 182, 230–238.

TELLA, S., PAUL, D., BERMAN, R.G., DAVIS, W.J., PETERSON, T.D., PEHRSSON, S.J., & KERSWILL, J.A. (2007) Bedrock geology compilation and regional synthesis of parts of Hearne and Rae domains, western Churchill Province, Nunavut-Manitoba. Geological Survey of Canada, Open File **5441**, scale 1:550,000 (3 sheets and a CD-ROM).

THORNE, W.S., HAGEMANN, S.G., WEBB, A., & CLOUT, J. (2008) Banded iron formation-related iron ore deposits of the Hamersley Province, Western Australia. *In* Banded Iron Formation-related High-Grade Iron Ore (S.G. Hagemann, A. Rosière, J. Gutzmer, & N.J. Beukes, eds.). *Reviews in Economic Geology* **15** (197–222).

THURSTON, P.C., KAMBER, B.S., & WHITEHOUSE, M. (2012) Archean cherts in banded iron formation: Insight into Neoarchean ocean chemistry and depositional processes. *Precambrian Research* **214–215**, 227–257.

WRIGHT, G.M. (1967) *Geology of the southeastern barren grounds, Parts of the Districts of Mackenzie and Keewatin*. Geological Survey of Canada, Memoire **350**, 91 pp.

ZHAO, W.W. & ZHOU, M.F. (2015) *In-situ* LA-ICP-MS trace elemental analyses of magnetite: the Mesozoic Tengtie skarn Fe deposit in the Nanling Range, South China. *Ore Geology Reviews* **65**, 872–883.

//titan/production/c/cami/live_jobs/cami-54/cami-54-03/cami-54-03-11/layouts/cami-54-03-11.3d
■ 4 January 2017 ■ 10:29 am ■ Allen Press, Inc.

Page 21

Queries for cami-54-03-11

This manuscript/text has been typeset from the submitted material. Please check this proof carefully to make sure there have been no font conversion errors or inadvertent formatting errors. Allen Press.